crystals

Article

Coercivity of $(Fe_{0.7}Co_{0.3})_2B$ Nanowire and Its Bonded Magnet

Xubo Liu * and **Ikenna C. Nlebedim**

Critical Materials Innovation Hub, Division of Critical Materials, Ames National Laboratory US DOE, Ames, IA 50011, USA; nlebedim@ameslab.gov
* Correspondence: liux@ameslab.gov

Abstract: $(Fe_{0.7}Co_{0.3})_2B$ are potential permanent magnets material due to its large saturation magnetization and high Curie temperature. However, it has moderate magnetocrystalline anisotropy (MCA) and low coercivity. One way to improve its coercivity is to combine the contributions from magnetocrystalline- and magnetic-shape anisotropy by preparing $(Fe_{0.7}Co_{0.3})_2B$ nanowires. We study the effects of size, morphology, and surface defects on the hard magnetic properties of nanowires using micromagnetic simulation. The hard magnetic properties of $(Fe_{0.7}Co_{0.3})_2B$ nanowire-bonded magnets are estimated, including the role of inter-wire magnetostatic interaction. By considering the existence of local reductions in MCA energy of up to 30% on the surface layer of nanowires, the anisotropic bonded magnet with a 65% vol. of $(Fe_{0.7}Co_{0.3})_2B$ nanowires would have typical remanence, B_r = 7.6–8.4 kG, coercivity, H_{ci} = 9.6–9.9 kOe, and maximum energy product, $(BH)_m$ = 14–17.8 MGOe. Developing effective technology for synthesizing nanowires and fabricating corresponding bonded magnets is promising for manufacturing practical magnets based on the magnetic phase with a relatively low or moderate MCA, such as $(Fe_{0.7}Co_{0.3})_2B$.

Keywords: magnetic anisotropy; coercivity; micromagnetic simulation; nanowire; Fe-Co-B

Citation: Liu, X.; Nlebedim, I.C. Coercivity of $(Fe_{0.7}Co_{0.3})_2B$ Nanowire and Its Bonded Magnet. *Crystals* **2024**, *14*, 624. https://doi.org/10.3390/cryst14070624

Academic Editor: John A. Mydosh

Received: 30 May 2024
Revised: 2 July 2024
Accepted: 3 July 2024
Published: 6 July 2024

1. Introduction

The high-performance permanent magnet market is almost wholly occupied by Nd-Fe-B and Sm-Co rare earth (RE) alloys that are used in many green energy fields, including electric vehicles and wind power generators [1,2]. The growth of the RE magnet market has resulted in a supply and demand bottleneck for critical RE metals such as Pr, Nd, Dy, and Tb. Hence, RE-free magnets have attracted more research attention in recent years [3–5]. Among the candidate materials for RE-free magnets, Fe-based compounds such as Fe-Co-B, Fe-Co-P, Fe-N, etc., are of great interest from a resource sustainability perspective [6–10].

The tetragonal phase $(Fe_{1-x}Co_x)_2B$ $(0.1 \leq x \leq 0.5)$ has an easy-axis magnetocrystalline anisotropy (MCA) with a peak value at x = 0.3 (MCA constant, K_1 = 4.1 Merg/cm^3, or magnetocrystalline anisotropy field, H_{MCA} = 7.8 kOe) at room temperature [10,11]. $(Fe_{0.7}Co_{0.3})_2B$ also has a large magnetization (Js = 13 kG) at room temperature and a high Curie temperature of 660 °C. Despite the good intrinsic magnetic properties of $(Fe_{0.7}Co_{0.3})_2B$ [12–16], its experimentally obtained coercivity is rather low at less than 100 Oe [14]. This low coercivity prevents Fe-Co-B from being used in practical applications. Kim et al. reported that doping heavy elements of Re can improve the coercivity of (Fe, Co, Re)$_2$B to about 900 Oe [15].

One way to enhance the coercivity of $(Fe_{0.7}Co_{0.3})_2B$ is to take advantage of its magnetic shape anisotropy (MSA) by controlling the particle sizes and shapes, just like in Alnico permanent magnets. Researchers developed nano-structural Alnico 80 years ago, and its magnetic anisotropy comes mainly from the shape magnetic anisotropy (K_s) of needle-shaped ferromagnetic Fe-Co precipitates distributed in a non-magnetic matrix phase of Ni-Al [17,18]. These needle-like Fe-Co particles have a 10–50 nm diameter and can be from several hundred to one thousand nanometers long [17,18]. Magnetic nanowires have been studied intensively in recent years [19–21]. Under proper synthesis conditions, hexagonal Cobalt nanowires can be made as single crystals, each with a single magnetic domain structure with a <001> crystallographic axis oriented along the length of the particles [21–23]. This gives rise to a uniaxial MCA (K_c) direction that coincides with the MSA (K_s) in the cobalt nanowires and results in a large effective anisotropy (K_{eff}), i.e., $K_{eff} = K_c + K_s$. Cobalt nanowires with a diameter (d) of 15 nm and a length (l) of 200 nm display a coercivity of about 10 kOe, which is higher than their theoretical magnetocrystalline anisotropy field (H_k = 7.6 kOe) [22]. The optimized bonded magnet of cobalt nanowire shows a magnetic remanence of B_r = 9.5 kG, coercivity of H_{ci} = 9.6 kOe, and maximum energy product of $(BH)_m$ = 20 MGOe [24]. However, the high cost of cobalt prevents it from being a practical magnet. It has been reported that Fe_2B nanowires with a diameter of about 30 nm can be deposited onto nickel foam via simple one-step chemical reduction in an externally applied magnetic field [25]. It has also been found that Co-Fe-B nanowires with a diameter of 175 nm and a length of 6–14 µm can be synthesized using electrodeposition with a nano-porous aluminate template [26]. Unfortunately, the array of Co-Fe-B nanowires shows a typical coercivity of 200 Oe due to the nanowires' large size [26]. These results indicate that Fe-Co-B nanowires can be synthesized, encouraging us to investigate the coercivity of $(Fe_{0.7}Co_{0.3})_2B$ nanowires and the potential magnetic performance of bonded magnets prepared with these nanowires.

In this work, we perform a micromagnetic simulation to elucidate the correlation of coercivity with the size, morphology, and surface defects of $(Fe_{0.7}Co_{0.3})_2B$ nanowires. The extrinsic magnetic properties, including remanence B_r, coercivity H_{ci}, and maximum energy product $(BH)_m$, are also calculated as a function of the packing fraction in $(Fe_{0.7}Co_{0.3})_2B$ nanowire-bonded magnets. Finally, the challenges and potential pathways for developing nanowire-based magnets are discussed.

2. Computational Method and Details

The micromagnetic simulation was based on the Landau–Lifshitz–Gilbert equation (LLG), which has been widely applied to simulate the magnetic properties of soft and hard magnets [27–29]. The micromagnetic simulations were performed using a finite difference GPU micromagnetic code, MuMax^3 (Version 3.10) [30,31]. Here, the finite difference cell size was 1 nm × 1 nm × 1 nm for all the calculations. The magnetic field step for calculating the magnetic hysteresis loop was 1 mT. Total energy minimization was performed using a conjugate gradient method with a converge criterion of a normalized magnetization change of less than 10^{-6}. The material parameters of $(Fe_{0.7}Co_{0.3})_2B$ for the micromagnetic simulations were derived from experiments [10]. The magnetization (M_s), magneto-crystalline anisotropy constant (K_1), and exchange constant (A_{ex}) were 1.035 kG, 4.1 Merg/cm^3, and 12×10^{-7} erg/cm, respectively.

3. Results

3.1. *Micromagnetic Simulation of Coercivity in $(Fe_{0.7}Co_{0.3})_2B$ Nanowires*

3.1.1. Coercivity of Defect-Free $(Fe_{0.7}Co_{0.3})_2B$ Nanowires

As a starting point, we used micromagnetic simulation to investigate the effects of size and morphology on the coercivity of ideal $(Fe_{0.7}Co_{0.3})_2B$ nanowires without any surface defects. Two typical nanowire shapes, prolate spheroid (s-nanowire) and cylinder (c-nanowire), were considered. The uniformly magnetized spheroid generates a uniform demagnetizing field, i.e., a demagnetizing field (H_d) that is homogeneous for s-nanowires, while it is non-uniform for c-nanowires. Theoretically, the maximum effective magnetic anisotropy field can be up to 14.3 kOe for an ideal single-crystal and single-magnetic-domain $(Fe_{0.7}Co_{0.3})_2B$ nanowire due to the contributions of MCA (H_{mca} = 7.8 kOe) and MSA ($H_{msa} = 1/2$, J_s = 6.5 kOe).

As shown in Figure 1, c-nanowires $(Fe_{0.7}Co_{0.3})_2B$ with a diameter of 32 nm (black solid sphere) showed a coercive field slightly higher than their theoretical magnetocrystalline anisotropic field (7.8 kOe), for the case in which the ratio between the length and diameter (l/d) was higher than 2, which was almost twice the value for l/d = 1 (4.3 kOe). Further increase in the *l*/*d* ratio had little effect on the coercivity (~8.1 kOe for *l*/*d* = 16). For the c-nanowire with half the diameter, i.e., 16 nm, the coercivity rapidly increased from 8.1 kOe (*l*/*d* = 1) to about 10.3 kOe (*l*/*d* = 2) and remained almost unchanged afterwards. It was unsurprising that the c-nanowire of 16 nm had a much higher coercivity than that of 32 nm. The critical domain diameter of $(Fe_{0.7}Co_{0.3})_2B$ sphere was about 22 nm, estimated based on the Brown formula $D = 7.211(A_{ex}/\mu_0)^{1/2}/Ms$ [32]. The parameters D, $A_{ex,}$ and Ms are the critical domain diameter, exchange constant, and saturation magnetization. A similar observation of a higher coercivity in nanowires with diameters less than the critical single domain size has also been made for cobalt nanowires [21,22]. For the same diameter (short axis diameter) and *l*/*d* ratio (i.e., the ratio between the long axis diameter and short axis diameter), the s-nanowires had a much higher coercivity than the c-nanowires. For a ratio of *l*/*d* = 16, s-nanowires with 16 nm and 32 nm diameters had coercivities of 14 kOe and 12 kOe, respectively. The calculated coercivity of the 16 nm nanowire was almost equal to the sum of the MCA field and the MSA field (14.3 kOe). Similar results have been experimentally observed for Co nanowires [22]. These values were higher than those for the c-nanowire with the same *l*/*d* ratio by about 40%. As shown in Figure 1, the coercivity values for c-nanowires with 16 nm and 32 nm diameters were 10.5 kOe and 8.2 kOe, respectively. These c-nanowires and s-nanowires can be the building blocks for bonded magnets or other composite permanent magnets.

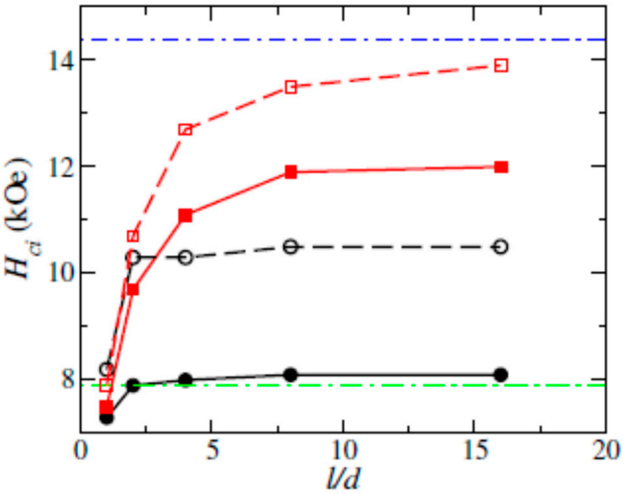

Figure 1. The calculated coercivities of c-nanowires (sphere) and s-nanowires (square) without structural defects. Open symbol: d = 16 nm, solid symbol: d = 32 nm. The dashed lines (green, bottom) and (blue, top) show the theoretical MCA field and total effective magnetic anisotropy field (sum of the contributions from MCA and MSA).

The big difference in coercivity values for the particles with different morphologies can be ascribed to their different magnetization and demagnetization field distributions. As shown in Figure 2a, the magnetization distributed almost homogeneously along the *z*-axis for a $(Fe_{0.7}Co_{0.3})_2B$ sphere with a diameter of 20 nm in a magnetic remanent state. The corresponding demagnetization was distributed along the opposite direction inside the sphere (Figure 2b). The sphere had a demagnetization factor of 1/3. The $(Fe_{0.7}Co_{0.3})_2B$ s-nanowires with a short axis diameter of 16 nm and a long axis diameter of 256 nm had an MCA easy-axis parallel to the long-axis direction (Figure 2c,d). Magnetization distributed homogeneously inside the s-nanowires (Figure 2c). The demagnetization field was stronger at the two ends than that at the middle part (Figure 2c). Overall, the demagnetization field aligned opposite to the magnetization direction. It slightly deviated from the z-direction (easy direction) near the surface at the two ends, which were the preferential nucleation sites for the magnetization reversal domains. For the c-nanowires $(Fe_{0.7}Co_{0.3})_2B$, the magnetization also almost completely aligned along the *z*-axis (Figure 2e). However, the demagnetization field was strong and deviated more substantially from the z-direction at the two ends of the c-nanowires (Figure 2f), compared to the s-nanowires (Figure 2d). The sharp edge of the c-nanowire ends (cylinder shape) caused strong demagnetization and was a preferential nucleation site for the magnetization reversal domain. This was one of the main reasons for the lower coercivity of the c-nanowire compared to the s-nanowire (Figure 1).

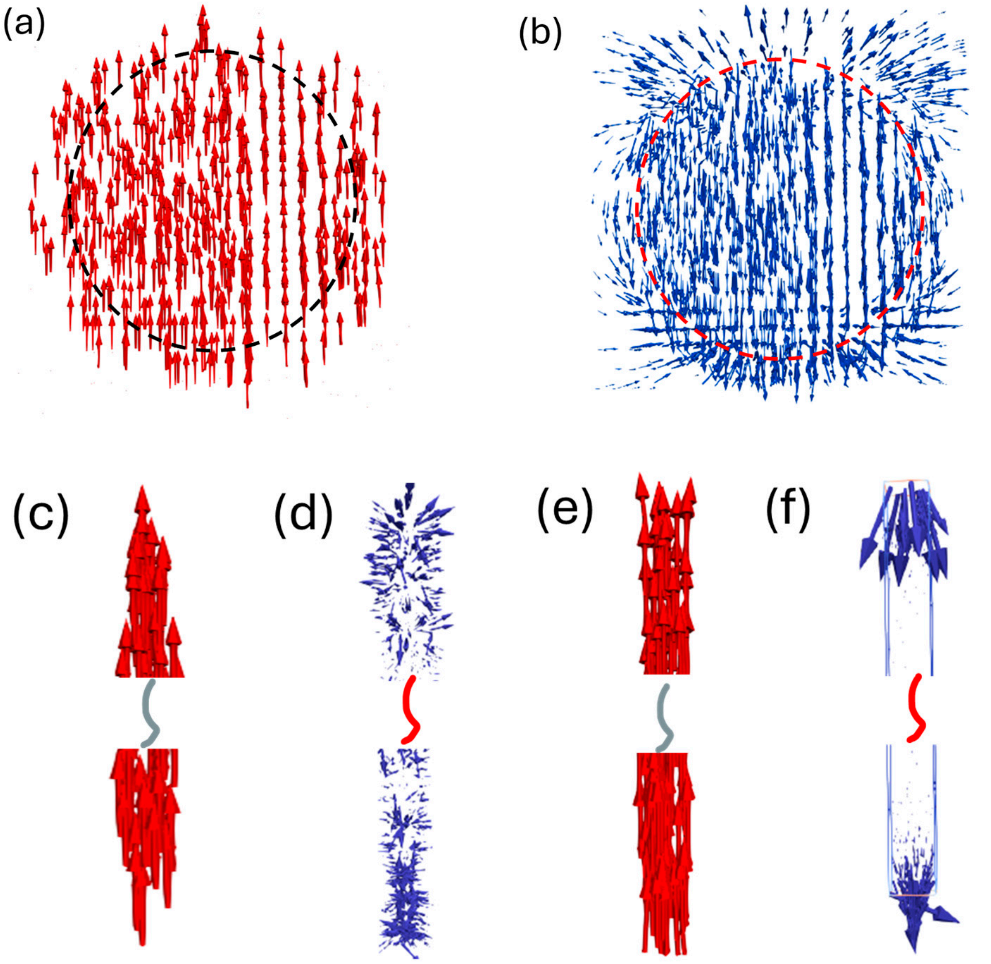

Figure 2. The magnetization (**a**,**c**,**e**) and demagnetization field (**b**,**d**,**f**) distribution of $(Fe_{0.7}Co_{0.3})_2B$ with a morphology of sphere (diameter 20 nm), s-nanowires (spheroid), and c-nanowire (cylinder) with a diameter of 16 nm and length of 256 nm at a magnetic remanent state (external field $H = 0$), respectively. Here, the arrows are the magnetization or demagnetization directions. The easy axis of magnetization is along the z-direction (vertical direction). Only the end parts (30 nm in length) of nanowires (**c**,**d**,**e**,**f**) are shown where the large changes in magnetization and demagnetization field were predicted.

3.1.2. Coercivity of $(Fe_{0.7}Co_{0.3})_2B$ Nanowires with Surface Defects

Our previous work indicated that the MCA of $(Fe_{0.7}Co_{0.3})_2B$ is sensitive to structural defects. A fluctuation in cobalt content of 10%, 1% isotropic lattice strain, or 2% tetragonal distortion reduces MCA energy up to 30% in $(Fe_{0.7}Co_{0.3})_2B$ [33]. Here, we studied the effects of a local weak MCA on the coercivity in s-nanowires and c-nanowires. As the particle surface had more structural defects than its core, we set up core–shell nanowire models, i.e., the nanowire core had an MCA of bulk single crystal ($K = 4.1$ Merg/cm^3) while the shell (2 nm thickness) had 10–30% less MCA (Figure 3).

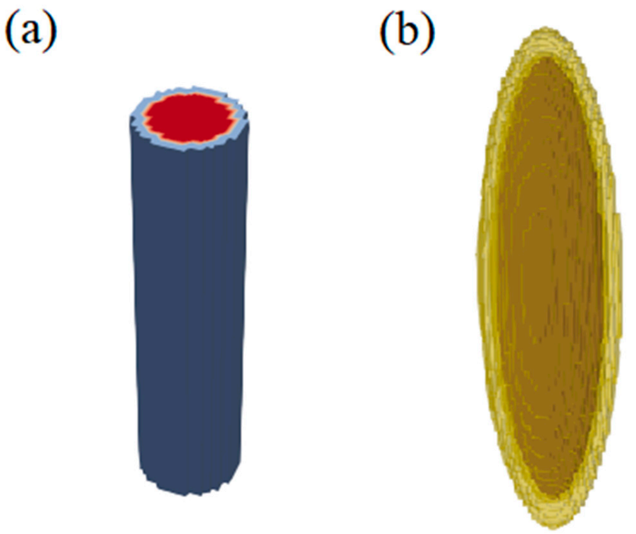

Figure 3. Scheme of core–shell geometry models for $(Fe_{0.7}Co_{0.3})_2B$ c-nanowire (**a**) and s-nanowire (**b**). The core and shell have MCA constants $K_1^{\ core}$ = 4.1 Merg/cm^3 and $K_1^{\ shell} = 0.7K_1^{\ core}$–$0.9K_1^{\ core}$, respectively.

Figure 4 displays the calculated coercivity as a function of the MCA constants of the shell layer, $K_1^{\ shell}$, in the $(Fe_{0.7}Co_{0.3})_2B$ c-nanowire (blue solid line) and s-nanowire (red, dashed line). With a decrease in the $K_1^{\ shell}$ value from 4.1 to 2.97 Merg/cm^3 (i.e., $K_1^{\ shell} = 0.7K_1^{\ core}$), the coercivity of the c-nanowire and s-nanowire decreased almost linearly from 10.5 to 9.4 kOe and from 14.1 to 12.9 kOe, respectively. The local reduction in MCA (nanowire surface) reduced the energy barrier for starting magnetization reversal, decreasing the coercivity.

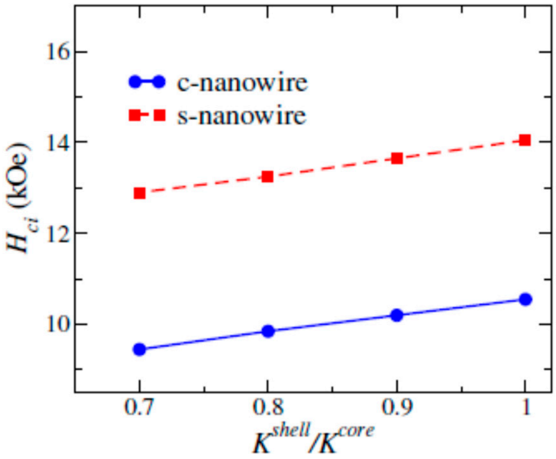

Figure 4. The calculated coercivity as a function of MCA constants of the shell layer, $K^{\ shell}$, in $(Fe_{0.7}Co_{0.3})_2B$ c-nanowire (blue solid line) and s-nanowire (red, dash line). The nanowires have diameters of 16 nm and lengths of 256 nm.

Table 1 lists the values of the calculated coercivities of some selective s-nanowires and c-nanowires. The remanence remained unchanged for different-sized c-nanowires and s-nanowires with and without a low MCA surface layer. Although the coercivity decreased with a decreasing $K_1^{\ shell}$, the values were still about 9.4 kOe and 13 kOe for the c-nanowires and s-nanowires with low MCA surface layers ($K_1^{\ shell} = 0.7K_1^{\ core}$). These values were higher than the theoretical maximum value contributed from the MCA (i.e., the MCA field H_K = 7.8 kOe). In other words, the magnetic shape anisotropy compensated for coercivity reduction due to local MCA fluctuations in the nanowires.

Table 1. Magnetic properties of nanowires with different thicknesses of surface defect layer (SFL). The MCA constant of SFT, $K_1^{shell} = 0.7K_1^{core}$. H_{ci}^{reduce} is the coercivity of nanowires with a magnetization reduction (10%).

	Size (nm)	**SFL Thickness (nm)**	H_{ci} **(kOe)**	H_{ci}^{reduce} **(kOe)**
c-nanowire	Φ16 × 256	0	10.5	10.1
c-nanowire	Φ16 × 256	1	9.9	9.6
c-nanowire	Φ16 × 256	2	9.4	9.1
c-nanowire	Φ32 × 256	0	8.2	8.0
s-nanowire	Φ16 × 256	0	14.1	13.8
s-nanowire	Φ16 × 256	1	13.3	13.1
s-nanowire	Φ16 × 256	2	12.9	12.7
s-nanowire	Φ32 × 256	0	12.0	11.8

Controlling the nanowire size and morphology can effectively improve the coercivity of the semi-hard magnetic phase lacking a strong MCA. All these nanowires had a coercivity higher than ½ of B_r, and the theoretical $(BH)_m$ could be estimated as $B_r^2/4$, or 42 MGOe (Br = 13.0 kG, bulk magnetization) without considering the ‘magnetization reduction effect’ of magnetic nanoparticles. A reduction in magnetization has been experimentally observed in magnetic nanoparticles, which was ascribed to the presence of a magnetically inactive surface [34]. The typical magnetization reduction is about 5–20%, depending on the surface-to-volume ratio in metallic ferromagnetic nanoparticles or nanowires [34]. Unfortunately, no reported experimental data on $(Fe,Co)_2B$ exist. For a 10% magnetization reduction, the Br and (BH)m values were reduced to 11.7 kG and 34 MGOe.

In addition to B_r and $(BH)_m$, the coercivity was also slightly changed by the ‘magnetization reduction effect’. On the one hand, reduced magnetization decreased the MSA, as did the coercivity that the MSA contributed. On the other hand, reduced magnetization lowered the demagnetization energy, increased the energy barrier for magnetization reversal, and somewhat enhanced the coercivity. The interplay between these two effects resulted in a slight decrease in coercivity by about 0.2–0.4 kOe for $(Fe,Co)_2B$ nanowires with different sizes and defect layers (Table 1).

Strictly speaking, the concept of $(BH)_m$ is only for bulk magnets. The $(BH)_m$ of the nanowires is the upper limit for a bulk magnet made from nanowires. However, assembling these nanowires into bulk magnets while retaining a high Br, Hci, and $(BH)_m$ remains challenging.

3.2. Coercivity of $(Fe_{0.7}Co_{0.3})_2B$ Bonded Magnet from Nanowires

The coercivity contributed by the MSA decreases with an increasing packing fraction of magnetic particles (or a decrease in the inter-particle distance) due to inter-particle magnetostatic interactions [35,36]. When the distance between neighboring nanowires is zero, the coercivity from the MSA disappears. Bonded magnets may be prepared using $(Fe_{0.7}Co_{0.3})_2B$ nanowires as the starting materials to take advantage of the coercivity contributed by magnetic shape anisotropy. Magnetic powder can be mixed with binders such as epoxy resin, nylon, etc., and formed into bulk magnets with specific shapes and sizes using methods like compression and injection molding [37]. The non-magnetic binder separates the magnetic nanowires in the bonded magnet, which helps to retain the coercivity originating from the MSA. In addition, the non-magnetic binder bonds the magnetic particles together, enabling the necessary mechanical properties for applications.

Although the bonded magnet can partially retain the coercivity contributed by magnetic shape anisotropy, the binder dilutes the magnetic powder content which, in turn, decreases the magnetic remanence and maximum energy product. To evaluate the potential performance of the $(Fe_{0.7}Co_{0.3})_2B$-bonded magnet, we calculated the magnetic properties as a function of the volume fraction of the particles. Four types of $(Fe_{0.7}Co_{0.3})_2B$ magnetic particles were selected as feedstock powders for the bonded magnet: (1) s-nanowire with a diameter of 16 nm and a length of 256 nm; (2) s-nanowire with a diameter of 16 nm and a length of 256 nm, including a surface defect layer of 2 nm with a reduced MCA of $K_1{}^{shell} = 0.7K_1{}^{core}$; (3) c-nanowire with a diameter of 16 nm and a length of 256 nm; and (4) c-nanowire with a diameter of 16 nm and a length of 256 nm, including a surface defect layer of 2 nm with reduced MCA of $K_1{}^{shell} = 0.7K_1{}^{core}$. The morphologies of the s-nanowire (3) and c-nanowire (4) with defects are also shown in Figure 3 and were described in the previous section. The nanowires were assumed to be magnetically aligned along a single direction and uniformly distributed in the bonded magnets.

The strong magnetostatic interactions between nanowires will reduce the coercivity of the assembly of magnetic nanowires. Several groups have studied the correlation between the coercivity and packing fraction for acicular-shaped magnetic particles [38–42]. The coercivity with contributions from the MCA and MSA can be approximated phenomenologically by [42]:

$$H_{ci}(P) = A + B(1 - P) \quad (1)$$

P, A, and B are the volume packing fractions, MCA-contributed coercivity, and isolated particle coercivity due to the MSA, respectively. For isolated particles ($P = 0$), the coercivity is the sum of the parts originating from the MCA and MSA. The predicted linear correlation between the coercivity and packing fraction from Equation (1) has also been confirmed in cobalt nanowire assemblies in micromagnetic simulations [43]. The coercivity value of several simulated nanowires with $K_1 = 0$ was calculated to derive parameter B. The shape, size, magnetization, and exchange parameters of the simulated nanowires were the same as those of nanowires 1, 2, 3, and 4, respectively. The calculated coercivity of the simulated nanowires was entirely contributed by magnetic shape anisotropy (i.e., B). Parameter A can be estimated from the coercivity difference between the actual and simulated nanowires. The calculated parameters A and B are listed in Table 2. The A values differed, but the B values were the same for nanowire 1 and nanowire 2. This result was unsurprising, as nanowires 1 and 2 had the same geometry, size, and magnetic parameters except for the MCA constant K_1. The parameter A was mainly determined by the MCA, while B arose from magnetic shape anisotropy. Similar observations were made for nanowire 3 and nanowire 4 (Table 2).

Table 2. Estimated parameters of A and B of $(Fe_{0.7}Co_{0.3})_2B$ particle.

Nanowires	Shape	Size (nm)	*A* (kOe)	*B* (kOe)	
1	s-nanowire	Φ16 × 256	7.9	6.1	
2	Core–shell s-nanowire	Core Φ 12 × 256 Shell thickness: 2	6.9	6.1	$K_1{}^{shell} = 0.7K_1{}^{core}$
3	c-nanowire	Φ16 × 256	7.45	3.1	
4	Core–shell c-nanowire	Core Φ 12 × 256 Shell thickness: 2	6.85	3.1	$K_1{}^{shell} = 0.7K_1{}^{core}$

Theoretically, the packing density for the orderly packing of ellipsoids is 0.7707 for particles with an aspect ratio larger than 1.732 [44]. The packing density of circular cylinders with a high aspect ratio is slightly higher than $\pi/\sqrt{12}$ (~ 0.9) based on geometry analysis [45]. So, we estimate the extrinsic magnetic properties of nanowire-bonded magnets with a packing fraction of up to 0.7. Figure 5 shows the calculated extrinsic magnetic properties of the $(Fe_{0.7}Co_{0.3})_2B$-bonded magnets with different types of particles. As expected, the coercivity decreased while the B_r values increased linearly with an increasing volume packing fraction. Relative to Equation (1) above, the coercivity originating from the MCA remained unchanged (A), while the coercivity arising from MSA linearly reduced with an increasing magnetic particle volume fraction. The B_r values of the bonded magnets were the same for different magnetic particles with the same volume fraction, since we assumed they had the same magnetization. As shown in Figure 5, all H_{ci} values were higher than half of the B_r values in these bonded magnets. The magnetic particles were assumed to be aligned entirely along their magnetic easy-axis direction, i.e., a 100% DOA (degree of alignment), resulting in a demagnetization curve with an excellent squareness in the bonded magnet. The $(BH)_m$ = $(B_r)^2/4$ showed a similar trend, being determined by the volume fraction of the different magnetic nanowires. For 40–70 vol.% c-nanowires with a 30% reduced MCA defect shell, the bonded magnets could achieve a H_{ci} value of ~7.3–8.2 kOe (Figure 5a), a B_r of 5.2–8.4 kGs (Figure 5b), and a $(BH)_m$ of 6.8–20.6 MGOe (Figure 5c). Considering the magnetization reduction (10%) due to the surface effect of the magnetic nanoparticles, the magnitude of B_r and $(BH)_m$ reduced to 4.7–8.2 kG (Figure 5b) and 5.5–16.7 MGOe (Figure 5c), respectively.

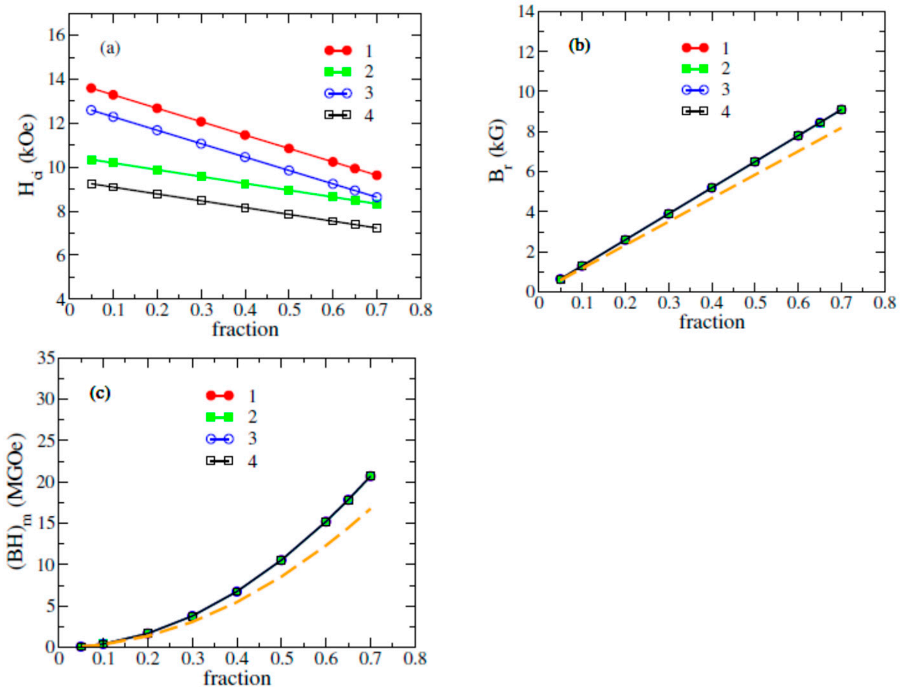

Figure 5. Calculated coercivity H_{ci} (**a**), magnetic remanence B_r (**b**), and maximum energy product $(BH)_m$ (**c**) as a function of volume packing fraction of $(Fe_{0.7}Co_{0.3})_2B$ nanowires in a bonded magnet. 1: s-nanowire; 2: s-nanowire with a surface defect layer of 2 nm; 3: c-nanowire; and 4: c-nanowire with a surface defect layer of 2 nm. The dashed lines show the dependence of B_r and $(BH)_m$ for the samples with 10% reduced magnetization, while other conditions remain same.

For the 40–70 vol.% s-nanowire with a 30% reduced MCA defect shell as feedstock, the bonded magnets would have a H_{ci} of 9.1–10.5 kOe and a $(BH)_m$ of 6.8–20.6 MGOe. Similar to the c-nanowire, a 10% magnetization reduction resulted in a smaller $(BH)_m$ of 5.5–16.7 MGOe in the s-nanowire-bonded magnets (Figure 5c). It should be noted that here, we considered only the perfect alignment situation (i.e., 100% DOA). However, misalignment of the nanowires would deteriorate the coercivity, remanence, and squareness of the demagnetization curves. The $(Fe_{0.7}Co_{0.3})_2B$-bonded magnets had a magnetic performance better than Sr- or Ba-ferrite and Alnico, comparable to Nd-Fe-B-bonded magnets, but inferior to sintered Nd-Fe-B and Sm-Co magnets. They can be potential gap magnets with a performance at an intermediate level between $SrFe_{12}O_{19}$ ferrite and Nd-Fe-B magnets.

3.3. Challenge and Roadmap for Developing $(Fe_{0.7}Co_{0.3})_2B$-Based Permanent Magnets

Due to the relatively low MCA of $(Fe_{0.7}Co_{0.3})_2B$, one way to improve its coercivity is to optimize its microstructure. Size and morphology significantly affect the coercivity of magnetic phases with a moderate or low MCA at the particle or crystal grain level. Appropriately tailored $(Fe_{0.7}Co_{0.3})_2B$ nanowires can achieve a coercivity higher than the theoretical value of the MCA field due to combining the contributions from MCA and MSA. This will potentially be a practical approach enabling the coercivity of hard magnetic phases with a moderate MCA, such as Fe-based magnets without rare earths. One challenge is effectively preparing $(Fe_{0.7}Co_{0.3})_2B$ nanowires on a large scale. Although there have been reports on the synthesis of Fe-Co-B magnetic micro- or nanowires in recent years [25,26], the synthesis of single-crystal and single-domain $(Fe_{0.7}Co_{0.3})_2B$ nanowires is still the most challenging task for developing Fe-Co-B hard magnets that leverage the combined contributions of MCA and MSA to coercivity. Developing novel synthesis technologies will be important in developing nanowire-based permanent magnets.

Another challenge is assembling the particles into bulk (full density or bonded) magnets. Figure 6a shows the schematic microstructure of a bonded magnet in which the $(Fe_{0.7}Co_{0.3})_2B$ nanowires retain their size and shape and are separated by the binder matrix. Hence, the coercivity of particles arising from the MSA can also be partially retained (Figure 5) since the binder helps to keep the particles separated. On the other hand, full-density bulk magnets would have a polycrystalline microstructure containing polyhedron grains with no specific morphology (Figure 6b). The coercivity originates from the MCA. Apart from the proper selection of binder and fabrication methods, one challenge for nanowire-bonded magnets is how to achieve a high DOA, which has a direct impact on the remanence, coercivity contributed from the MSA part, squareness of the demagnetization curve, and maximum energy product.

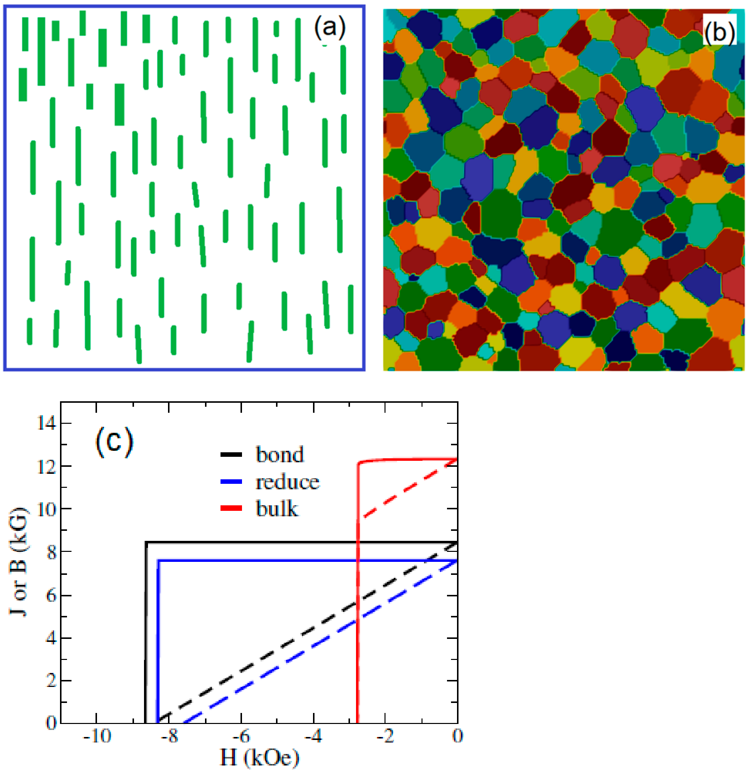

Figure 6. Microstructure model of nanowire-bonded magnet (**a**) and fully dense polycrystalline bulk magnet (**b**) of $(Fe_{0.7}Co_{0.3})_2B$ and their calculated demagnetization curves (*J-H* and *B-H*) (**c**). The polycrystalline bulk magnet has a mean grain size of 20 nm and a fluctuation of MCA energy of 30% between different grains. The bonded magnet has a volume fraction of 70% for s-nanowire ($\Phi 16 \times 256$ nm). The s-nanowire has a surface defect layer (2 nm thickness) with a reduced MCA constant $K_1^{shell} = 0.7 K_1^{core}$. In (**c**), the solid and dashed lines are for *J-H* and *B-H*, respectively. The *J-H* (*B-H*) curve of 'reduce' (blue) is calculated for the nanowire bonded magnet as (**b**), but with a 10% magnetization reduction. See more details in the main text.

Figure 6c shows the calculated demagnetization curves for the nanowire-bonded magnet and full-density polycrystalline magnet. The bonded magnet had a 65 vol% of $(Fe_{0.7}Co_{0.3})_2B$ s-nanowires (Figure 6a). The s-nanowire had a size of $\Phi 16 \times 256$ nm and a 2 nm thick surface shell with an MCA reduction of 30%. This would result in a bonded magnet with B_r = 8.4 kG, H_{ci} = 9.9 kOe, and $(BH)_m$ = 17.8 MGOe (Figure 6c). If we considered a potential magnetization reduction of 10% due to the surface effect of nanowires, the corresponding bonded magnet would have a B_r of 7.6 kG, H_{ci} = 9.6 kOe and a $(BH)_m$ of 14 MGOe (Figure 6c), comparable with an anisotropic Nd-Fe-B-bonded magnet. The large coercivity enabled a linear second quadrant induction demagnetization B-H curve with no knee point (Figure 6c, black and blue dash lines). Such a B-H curve is ideal for dynamic applications, e.g., electric motors and generators.

The full-density polycrystalline bulk magnet had a mean grain size of 20 nm, a local MCA reduction of up to 30% (Figure 6b), and showed typical extrinsic magnetic properties of B_r = 12.3 kG, H_{ci} = 2.7 kOe, and $(BH)_m$ = 25.6 MGOe in the micromagnetic simulation (Figure 6c). Although it can result in a higher B_r and $(BH)_m$, the low intrinsic coercivity resulted in a nonlinear second quadrant induction demagnetization curve (B-H curve) with a knee point in the second quadrant of the hysteresis loop. This limits them to some static applications (i.e., the working point is fixed).

4. Summary

$(Fe_{0.7}Co_{0.3})_2B$ displays promising intrinsic magnetic properties, including a large magnetization, high Curie temperature, and moderate MCA. For rationally tailored sizes and morphologies of $(Fe_{0.7}Co_{0.3})_2B$ nanowires, their coercivity can be up to 10–14 kOe due to the combined contributions of the MCA and MSA. A typical anisotropic bonded magnet, with a 65 vol.% of $(Fe_{0.7}Co_{0.3})_2B$ nanowire and a linear second quadrant induction demagnetization B-H curve, would have B_r = 7.6–8.4 kG, H_{ci} = 9.6–9.9 kOe, and $(BH)_m$ = 14–17.8 MGOe. Such properties are well-suited for dynamic applications such as electric motors and generators. The method used in the present work has good potential as an effective approach for developing permanent magnets using compositions with moderate MCA constant values. The challenge that needs to be overcome is how to effectively prepare nanowires with single-crystal and single-magnetic-domain structures, and how to assemble them into bulk magnets. Developing novel synthesis techniques that enable size and morphology control is highly needed to address the stated challenge and enable practical application of nanowire-based permanent magnets.

Author Contributions: Conceptualization, X.L. and I.C.N.; methodology, X.L. and I.C.N.; software, X.L.; validation, X.L. and I.C.N.; formal analysis, X.L. and I.C.N.; investigation, X.L.; resources, I.C.N.; data curation, X.L.; writing—original draft preparation, X.L.; writing—review and editing, I.C.N.; visualization, X.L.; supervision, I.C.N.; project administration, X.L. and I.C.N.; funding acquisition, X.L. and I.C.N. All authors have read and agreed to the published version of the manuscript.

Funding: This research was funded by the Critical Materials Innovation Hub funded by the U.S. Department of Energy, Office of Energy Efficiency and Renewable Energy, Advanced Materials and Manufacturing Technologies Office (AMMTO). The work was performed in Ames National Laboratory, operated for the U.S. Department of Energy by Iowa State University of Science and Technology under Contract No. DE-AC02-07CH11358.

Data Availability Statement: The original contributions presented in the study are included in the article, further inquiries can be directed to the corresponding author.

Conflicts of Interest: The authors declare no conflicts of interest.

References

1. Coey, J.M.D. Perspective and Prospects for Rare Earth Permanent Magnets. *Engineering* **2020**, *6*, 119–131. [CrossRef]
2. Gutfleisch, O.; Willard, M.A.; Brück, E.; Chen, C.H.; Sankar, S.G.; Liu, J.P. Magnetic Materials and Devices for the 21st Century: Stronger, Lighter, and More Energy Efficient. *Adv. Mater.* **2011**, *23*, 821–842. [CrossRef] [PubMed]
3. Coey, J.M.D. Permanent Magnets: Plugging the Gap. *Scr. Mater.* **2012**, *67*, 524–529. [CrossRef]
4. Kramer, M.J.; McCallum, R.W.; Anderson, I.A.; Constantinides, S. Prospects for Non-Rare Earth Permanent Magnets for Traction Motors and Generators. *JOM* **2012**, *64*, 752–763. [CrossRef]

5. Cui, J.; Kramer, M.; Zhou, L.; Liu, F.; Gabay, A.; Hadjipanayis, G.; Balasubramanian, B.; Sellmyer, D. Current Progress and Future Challenges in Rare-Earth-Free Permanent Magnets. *Acta Mater.* **2018**, *158*, 118–137. [CrossRef]
6. Mohapatra, J.; Liu, X.; Joshi, P.; Liu, J.P. Hard and Semi-Hard Fe-Based Magnetic Materials. *J. Alloys Compd.* **2023**, *955*, 170258. [CrossRef]
7. Yibole, H.; Lingling-Bao, B.; Xu, J.Y.; Alata, H.; Tegus, O.; Hanggai, W.; van Dijk, N.H.; Brück, E.; Guillou, F. (Fe,Co)$_2$(P,Si) Rare-Earth Free Permanent Magnets: From Macroscopic Single Crystals to Submicron-Sized Particles. *Acta Mater.* **2021**, *221*, 117388. [CrossRef]
8. Yin, L.; Juneja, R.; Lindsay, L.; Pandey, T.; Parker, D.S. Semihard Iron-Based Permanent-Magnet Materials. *Phys. Rev. Appl.* **2021**, *15*, 024012. [CrossRef]
9. Wang, J.-P. Environment-Friendly Bulk Fe16N2 Permanent Magnet: Review and Prospective. *J. Magn. Magn. Mater.* **2019**. [CrossRef]
10. Coene, W.; Hakkens, F.; Coehoorn, R.; de Mooij, D.B.; de Waard, C.; Fidler, J.; Grössinger, R. Magnetocrystalline Anisotropy of Fe$_3$B, Fe$_2$B and Fe$_{1.4}$Co$_{0.6}$B as Studied by Lorentz Electron Microscopy, Singular Point Detection and Magnetization Measurements. *J. Magn. Magn. Mater.* **1991**, *96*, 189–196. [CrossRef]
11. Iga, A. Magnetocrystalline Anisotropy in (Fe$_{1\text{-}x}$Co$_x$)$_2$ B System. *Jpn. J. Appl. Phys.* **1970**, *9*, 415–416. [CrossRef]
12. Kuz'min, M.D.; Skokov, K.P.; Jian, H.; Radulov, I.; Gutfleisch, O. Towards High-Performance Permanent Magnets without Rare Earths. *J. Phys. Condens. Matter* **2014**, *26*, 064205. [CrossRef] [PubMed]
13. Edström, A.; Werwiński, M.; Iuşan, D.; Rusz, J.; Eriksson, O.; Skokov, K.P.; Radulov, I.A.; Ener, S.; Kuz'Min, M.D.; Hong, J.; et al. Magnetic Properties of (Fe$_{1\text{-}X}$Co$_X$)$_2$ B Alloys and the Effect of Doping by 5d Elements. *Phys. Rev. B Condens. Matter Mater. Phys.* **2015**, *92*, 174413. [CrossRef]
14. Lamichhane, T.N.; Palasyuk, O.; Antropov, V.P.; Zhuravlev, I.A.; Belashchenko, K.D.; Nlebedim, I.C.; Dennis, K.W.; Jesche, A.; Kramer, M.J.; Bud'ko, S.L.; et al. Reinvestigation of the Intrinsic Magnetic Properties of (Fe1-XCox)2B Alloys and Crystallization Behavior of Ribbons. *J. Magn. Magn. Mater.* **2020**, *513*, 167214. [CrossRef]
15. Kim, K.M.; Kwon, H.W.; Lee, J.G.; Yu, J.H. Coercivity and Phase Evolution in Mechanically Milled (FeCo)$_2$ B-Type Hard Magnetic Alloy. *IEEE Trans. Magn.* **2018**, *54*, 1–5. [CrossRef]
16. Wallisch, W.; Fidler, J.; Toson, P.; Sassik, H.; Svagera, R.; Bernardi, J. Synthesis and Characterisation of (Fe,Co)$_2$–3B Microcrystalline Alloys. *J. Alloys Compd.* **2015**, *644*, 199–204. [CrossRef]
17. Campbell, R.B.; Julien, C.A. Structure of Alnico v. *J. Appl. Phys.* **1961**, *32*, S192–S194. [CrossRef]
18. Zhou, L.; Miller, M.K.; Lu, P.; Ke, L.; Skomski, R.; Dillon, H.; Xing, Q.; Palasyuk, A.; McCartney, M.R.; Smith, D.J.; et al. Architecture and Magnetism of Alnico. *Acta Mater.* **2014**, *74*, 224–233. [CrossRef]
19. Ortega, E.; Reddy, S.M.; Betancourt, I.; Roughani, S.; Stadler, B.J.H.; Ponce, A. Magnetic Ordering in 45 Nm-Diameter Multisegmented FeGa/Cu Nanowires: Single Nanowires and Arrays. *J. Mater. Chem. C Mater.* **2017**, *5*, 7546–7552. [CrossRef]
20. Zighem, F.; Mercone, S. Magnetization Reversal Behavior in Complex Shaped Co Nanowires: A Nanomagnet Morphology Optimization. *J. Appl. Phys.* **2014**, *116*, 193904. [CrossRef]
21. Maurer, T.; Ott, F.; Chaboussant, G.; Soumare, Y.; Piquemal, J.-Y.; Viau, G. Magnetic Nanowires as Permanent Magnet Materials. *Appl. Phys. Lett.* **2007**, *91*, 172501. [CrossRef]
22. Gandha, K.; Elkins, K.; Poudyal, N.; Liu, X.; Liu, J.P. High Energy Product Developed from Cobalt Nanowires. *Sci. Rep.* **2014**, *4*, 5345. [CrossRef] [PubMed]
23. Dumestre, F.; Chaudret, B.; Amiens, C.; Fromen, M.-C.; Casanove, M.-J.; Renaud, P.; Zurcher, P. Shape Control of Thermodynamically Stable Cobalt Nanorods through Organometallic Chemistry. *Angew. Chem. Int. Ed.* **2002**, *41*, 4286–4289. [CrossRef]
24. Mohapatra, J.; Xing, M.; Elkins, J.; Beatty, J.; Liu, J.P. Extraordinary Magnetic Hardening in Nanowire Assemblies: The Geometry and Proximity Effects. *Adv. Funct. Mater.* **2021**, *31*, 2010157. [CrossRef]
25. Liu, Q.; Zhao, H.; Jiang, M.; Kang, Q.; Zhou, W.; Wang, P.; Zhou, F. Boron Enhances Oxygen Evolution Reaction Activity over Ni Foam-Supported Iron Boride Nanowires. *J. Mater. Chem. A Mater.* **2020**, *8*, 13638–13645. [CrossRef]
26. Beron, F.; Clime, L.; Ciureanu, M.; Menard, D.; Cochrane, R.W.; Yelon, A. First-Order Reversal Curves Diagrams of Ferromagnetic Soft Nanowire Arrays. *IEEE Trans. Magn.* **2006**, *42*, 3060–3062. [CrossRef]
27. Brown, W.F., Jr. *Micromagnetics*; Wiley: New York, NY, USA, 1963.
28. Fidler, J.; Schrefl, T. Micromagnetic Modelling—The Current State of the Art. *J. Phys. D Appl. Phys.* **2000**, *33*, R135–R156. [CrossRef]
29. Durst, K.-D.; Kronmüller, H. The Coercive Field of Sintered and Melt-Spun NdFeB Magnets. *J. Magn. Magn. Mater.* **1987**, *68*, 63–75. [CrossRef]
30. Vansteenkiste, A.; De Wiele, B.V. Mumax: A New High-Performance Micromagnetic Simulation Tool. *J. Magn. Magn. Mater.* **2011**, *323*, 2585–2591. [CrossRef]
31. Vansteenkiste, A.; Leliaert, J.; Dvornik, M.; Helsen, M.; Garcia-Sanchez, F.; van Waeyenberge, B. The Design and Verification of MuMax3. *AIP Adv.* **2014**, *4*, 107133. [CrossRef]
32. Brown, W.F. The fundamental theorem of the theory of fine ferromagnetic particles. *Ann. N. Y. Acad. Sci.* **1969**, *147*, 463–488. [CrossRef]
33. Liu, X.B.; Nlebedim, I.C. Robustness of Magnetocrystalline Anisotropy and Coercivity in Fe–Co–B. *Phys. B Condens. Matter* **2024**, *683*, 415914. [CrossRef]

34. Ma, Z.; Mohapatra, J.; Wei, K.; Liu, J.P.; Sun, S. Magnetic Nanoparticles: Synthesis, Anisotropy, and Applications. *Chem. Rev.* **2023**, *123*, 3904–3943. [CrossRef] [PubMed]
35. Coey, J. *Magnetism and Magnetic Materials*; Cambridge University Press: Cambridge, UK, 2010.
36. Gong, M.; Dai, Q.; Ren, S. Magnetic Dipolar Interaction Induced Cobalt Nanowires. *Nanotechnology* **2016**, *27*, 07LT02. [CrossRef] [PubMed]
37. Nlebedim, I.C.; Ucar, H.; Hatter, C.B.; McCallum, R.W.; McCall, S.K.; Kramer, M.J.; Paranthaman, M.P. Studies on in Situ Magnetic Alignment of Bonded Anisotropic Nd-Fe-B Alloy Powders. *J. Magn. Magn. Mater.* **2017**, *422*, 168–173. [CrossRef]
38. Knowles, J. Packing Factor and Coercivity in Tapes: A Monte Carlo Treatment. *IEEE Trans. Magn.* **1985**, *21*, 2576–2582. [CrossRef]
39. Lyberatos, A.; Wohlfarth, E.P. A Monte Carlo Simulation of the Dependence of the Coercive Force of a Fine Particle Assembly on the Volume Packing Factor. *J. Magn. Magn. Mater.* **1986**, *59*, L1–L4. [CrossRef]
40. Chang, C.-R.; Shyu, J.-P. Particle Interaction and Coercivity for Acicular Particles. *J. Magn. Magn. Mater.* **1993**, *120*, 197–199. [CrossRef]
41. Skomski, R.; Liu, Y.; Shield, J.E.; Hadjipanayis, G.C.; Sellmyer, D.J. Permanent Magnetism of Dense-Packed Nanostructures. *J. Appl. Phys.* **2010**, *107*, 09A739. [CrossRef]
42. Knowles, J.E. Coercivity and Packing Density in Acicular Particles. *J. Magn. Magn. Mater.* **1981**, *25*, 105–112. [CrossRef]
43. Panagiotopoulos, I.; Fang, W.; Ott, F.; Boué, F.; Aït-Atmane, K.; Piquemal, J.-Y.; Viau, G. Packing Fraction Dependence of the Coercivity and the Energy Product in Nanowire Based Permanent Magnets. *J. Appl. Phys.* **2013**, *114*, 143902. [CrossRef]
44. Donev, A.; Stillinger, F.H.; Chaikin, P.M.; Torquato, S. Unusually Dense Crystal Packings of Ellipsoids. *Phys. Rev. Lett.* **2004**, *92*, 255506. [CrossRef] [PubMed]
45. Kusner, W. Upper Bounds on Packing Density for Circular Cylinders with High Aspect Ratio. *Discret. Comput. Geom.* **2014**, *51*, 964–978. [CrossRef]